Dyes and Pigments 232 (2025) 112440

Contents lists available at ScienceDirect

Dyes and Pigments

journal homepage: www.elsevier.com/locate/dyepig

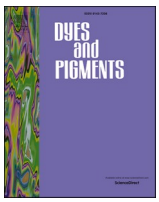

Strong and pH dependent fluorescence in unprecedented anthra[2,3-*d*] imidazole derivatives

Emmanuele Parisi [a], Emanuela Santagata [b], Alessandro Landi [c], Roberto Centore [b], Marco Chino [b], Antonio Carella [b,*]

[a] *Department of Applied Science and Technology, Politecnico di Torino Corso Duca degli Abruzzi 24, Torino, Italy*
[b] *Department of Chemical Sciences Università degli Studi di Napoli Federico II Via Cinthia 26, Napoli, Italy*
[c] *Dipartimento di Chimica e Biologia "Adolfo Zambelli", University of Salerno, Via Giovanni Paolo II, I-84084, Fisciano, SA, Italy*

A R T I C L E I N F O

Keywords:
Anthraimidazole
Fluorescence
pH sensors
XRD diffraction
Anthraquinone derivatives

A B S T R A C T

We here report the synthesis and characterization of three new molecules based on an unprecedented anthra [2,3-*d*]imidazole unit. The new heterocycle was unexpectedly formed while attempting to obtain 2,3-diacetamidoanthracene by reducing the corresponding anthraquinone molecules by sodium borohydride. The same reaction was successfully performed using two further different 2,3-diamidoanthraquinone derivatives, thus confirming its generality. The chemical identity of the novel molecules was also proved by realizing single crystals suitable for XRD diffraction and solving the crystalline structure of one of the prepared systems. All the molecules are strong blue emitters in ethanol, with fluorescence quantum yields around 0.40. Because of the acid-base properties of anthraimidazole ring, the optical response was investigated at different pH values. While slight differences were observed in acidic conditions, in the alkaline pH range we observed a dramatic change of the fluorescence spectra in a narrow pH range (from 11 to 13), with the color of the emission turning from blue to green. This feature makes the new class of derivatives here reported very promising as pH sensors working in strongly alkaline conditions.

1. Introduction

Anthracene and its derivatives have attracted a great deal of interest because of their interesting fluorescence properties [1]: several studies on the use of anthracene derivatives as OLED emitters are reported in the literature [2–5]; at the same time aromatic hydrocarbon compounds have been widely investigated as fluorescent sensors, especially for the detection of metal ions [6–10] and biological molecules [11,12]. Anthracene derivatives are more recently gaining a growing interest as organic semiconductors [13]: the planar conjugated structure, the strong intermolecular interactions and the higher solubility and stability as compared to other linear acenes, made anthracene a useful scaffold for the synthesis of high-performance organic materials for OFET [14–16] and OLET [17,18]. Anthracene derivatives are typically realized by functionalizing the ring in position 9,10 (the more reactive sites towards electrophilic substitution) or in positions 2,6, typically starting from 2,6-diaminoanthraquinone. Rarer are derivatives in which anthracene is fused with heterocyclic rings to obtain linear extended polycyclic heteroaromatic compounds [19–21], this being at variance with lower analogues like naphthalene and benzene [22–26]. In the wide realm of possible heterocycles, imidazole appears as a promising candidate: imidazole ring is ubiquitous in nature and its ability to bond to metals as a ligand and to form hydrogen bond with drugs and proteins, led to the development of a plethora of new derivatives for applications in medicinal chemistry [27,28]. In particular, new interesting molecular systems have been prepared by fusing imidazole with phenanthrene moieties, affording promising luminescent materials that have been efficiently used in OLED [29,30] and in Light Emitting Electro-chemical cells (LEC) [31–33]. Moreover, an interesting feature of imidazole unit relies on its basic (pyridine like nitrogen) and acid (pyrrole like N–H) functionalities: this property have been used to realized pH-dependent sensors based on phenanthroimidazole derivatives [34–36]. The combination of the fluorescence properties of anthracene unit with the acid base properties of imidazole ring could afford interesting pH dependent sensors but, up to date, to our knowledge, linear anthraimidazole derivatives have never been reported. With

* Corresponding author.
E-mail addresses: emmanuele.parisi@polito.it (E. Parisi), antonio.carella@unina.it (A. Carella).

https://doi.org/10.1016/j.dyepig.2024.112440
Received 10 July 2024; Received in revised form 8 September 2024; Accepted 8 September 2024
Available online 10 September 2024

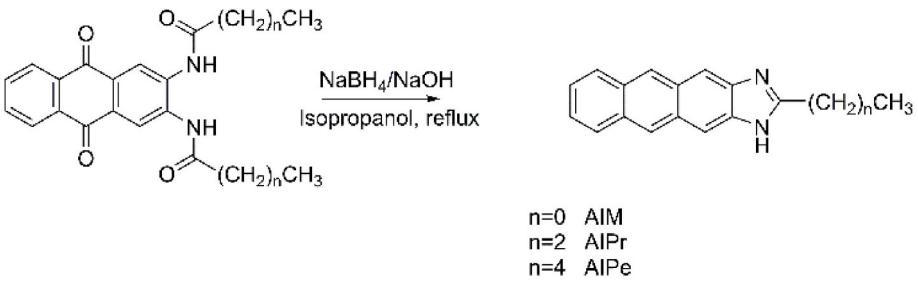

Scheme 1. Serendipitous reaction for the synthesis of unprecedented anthraimidazole derivatives.

the aim of synthesizing 2,3-diaminoanthracene starting from 2,3-diamino-9,10-anthraquinone, we explored the possibility of using a procedure previously reported in the literature, used for the preparation of 2,6-diaminoanthracene [37]. In that work, 2,6-diaminoanthraquinone was firstly acylated to obtain the corresponding diamide compound, and then treated with $NaBH_4$ to reduce anthraquinone to anthracene; a final hydrolysis led to the desired diamino derivative. We applied the same procedure to our substrate, 2,3-diaminoanthraquinone, acetylating the amino groups and then reacting the diacetamido compound with $NaBH_4$. To our surprise, we found that the reaction afforded in a moderate yield an unprecedented anthra [2,3-*d*] imidazole derivative, functionalized in the peripheral carbon of imidazole ring, with a methyl group (**AIM**, see Scheme 1).

To assess the generality of the reaction, we repeated it by preparing and reacting two different dialkylamido derivatives (dibutylamido and dihexylamido analogues), and the anthraimidazole cycle was again formed with, respectively, a propyl (**AIPr**) and a pentyl tail (**AIPe**). The chemical identity of the new compounds was confirmed by NMR spectroscopy and high-resolution mass spectrometry (HR-MS). All the new compounds were characterized regarding their absorption and fluorescence properties, that resulted in quite similar behaviour. The anthraimidazole ring is characterized by acid and basic nitrogen and hence, an analysis of the dependence of optical properties on pH was performed, exclusively for what concerns AIM molecule. Moreover, a DFT study of the electronic properties of AIM has been performed. Finally, structural properties of **AIM** molecule were moreover studied in detail: single crystals of **AIM** and of its hydrobromide salt (**AIM•HBr**) were prepared, and their crystalline structure were solved by means of XRD analysis.

2. Experimental section

2.1. General information

All reagents were purchased with analytical grade and were used without further purification. 2,3-diaminoanthraquinone (**DA-AQ**) was synthesized according to a previously reported paper (NMR spectra in SI, Figs. S1–S2) [38]. Compounds' identity was confirmed by Bruker Avance 400 MHz, NMR spectrometer. 1H NMR and 13C NMR spectra were recorded by using DMSO-d_6 solvent and d_6-Acetone. FTIR spectra were recorded dispersing the dye in KBr pellets and using a JASCO FTIR 4700 spectrometer. Differential scanning calorimetric (DSC) analysis was performed using a Mettler Toledo DSC 3 instrument, under flowing nitrogen, at 10 K•min^{-1} scanning rate. UV/Vis and PL spectra were recorded with a Jasco V750 and Jasco FP-750 spectrophotometers at 200 nm/min scanning speed. Fluorescence quantum yield quantum yield was calculated by using the quinine sulphate as standard [39]. ESI-IT/TOF spectra were recorded on a Shimadzu LCMS-IT-TOF system with ESI interface and Shimadzu LC-MS solution Workstation software for the data. The optimized MS parameters were selected as followed: CDL (curved desolvation line) temperature 200 °C; the block temperature 200 °C; the probe temperature 200 °C; detector gain 1.7 kV; probe voltage +4.5 kV; CDL voltage −15 V. Nitrogen served as nebulizer gas (flow rate: 1.5 L min^{-1}). Electrochemical characterization was performed by means of cyclic voltammetry (CV) using a BioLogic sp150 potentiostat. The samples were analyzed in acetonitrile solution in a three-electrode set-up, with a Au working electrode and a Pt wire counter-electrode while Ag/AgCl was used as the reference electrode. Electrolyte consisted in a tetrabutylammonium hexafluorophosphate 0.1 M solution in acetonitrile. CV were conducted at 100 mV/s. The found potential values were referred to Fc/Fc^+ acting as internal standard. Before each measurement, the electrolyte was degassed with Argon to avoid the presence of oxygen.

2.2. Synthesis

2.2.1. Synthesis of 2,3-diacetamidoanthraquinone (AQ-DA-Ac)

2,3-diaminoanthraquinone (2 g, 8.4 mmol) was suspended in dry toluene (80 mL) and acetic anhydride (7.67 g, 75 mmol) was added to the suspension. The reaction was left at reflux for 24 h under nitrogen flux. Afterwards the mixture was cooled and filtered under vacuum. 1.9 g (5.89 mmol) of a yellowish solid were isolated. Yield 70 %. M. p. 334 °C **^{1}H-NMR** (DMSO-d_6, 400 MHz): δ 2.17 (s, 6H), 7.90 (m, 2H), 8.18 (m, 2H), 8.63 (s, 2H) 11.06 (s, broad, 2H); **^{13}C-NMR** (100 MHz, DMSO-d_6) δ 24.4, 121.8, 127.1, 129.1, 133.7, 134.7, 135.6, 170.1, 182.2. FTIR (KBr, cm^{-1}): ν = 3435 (br, N–H), 3246, (w, C–H arom.), 1659 (s, C═O), 1557 (w), 1328 (m), 1237 (m), 712 (m, C–H bending). Elemental analysis calcd for $C_{18}H_{16}N_2O_2$: C 73.95, H 5.52, N 9.58, found: C 74.11, H 5.60, N 9.50.

2.2.2. Synthesis of 2,3-dibutylamidoanthraquinone (AQ-DA-Bu)

2,3-diaminoanthraquinone (2 g, 8.4 mmol) was suspended in dry toluene (80 mL) and butyric anhydride (11.86 g, 75 mmol) was added to the suspension. The reaction was left at reflux for 24 h under nitrogen flux. Afterwards the mixture was cooled and filtered under vacuum. The obtain solid was washed with methyl alcohol (100 mL) and filtered again 2.0 g (5.29 mmol) of a yellowish solid were isolated. Yield 63 % M. p. 240 °C. **^{1}H-NMR** (DMSO-d_6, 400 MHz): δ 0.97 (t, 6H, J = 7.5 Hz), 1.67 (m, 4H), 2.43 (t, 4H, J = 7.5 Hz); 7.91 (m, 2H), 8.19 (m, 2H), 8.54 (s, 2H) 11.06 (s, broad, 2H). **^{13}C-NMR** (100 MHz, DMSO-d_6) δ 14.1, 18.8, 38.6, 122.4, 127.2, 129.6, 133.7, 134.8, 135.5, 172.5, 182.1. FTIR (KBr, cm^{-1}): ν = 3454 (br, N–H), 3312, (C–H arom.), 2964 (C–H aliph.) 1677 (s, C═O), 1581, 1337, 1247, 707 (m, C–H bending). Elemental analysis calcd for $C_{22}H_{24}N_2O_2$: C 75.83, H 6.94, N 8.04, found: C 75.99, H 6.85, N 7.98.

2.2.3. Synthesis of 2,3-dihexylamidoanthraquinone (AQ-DA-Hex)

2,3-diaminoanthraquinone (2 g, 8.4 mmol) was suspended in dry toluene (80 mL) and hexanoic anhydride (16.1 g, 75 mmol) was added to the suspension. The reaction was left at reflux for 24 h under nitrogen flux. Afterwards the mixture was cooled to RT and then in an ice water bath for 30 min. The system was then filtered under vacuum. The obtain solid was washed with methyl alcohol (100 mL) and filtered again 2.2 g (5.06 mmol) of a greenish solid were isolated. Yield 60 %. M. p. 226 °C **^{1}H-NMR** (DMSO-d_6, 400 MHz): δ 0.90 (t, 6H, J = 7.5 Hz), 1.34 (m, 8H), 1.65 (m, 4H), 2.45 (t, 4H, J = 7.5 Hz); 7.92 (m, 2H), 8.20 (m, 2H), 8.53 (s, 2H) 11.06 (s, broad, 2H); **^{13}C-NMR** (100 MHz, DMSO-d_6) δ 14.3,

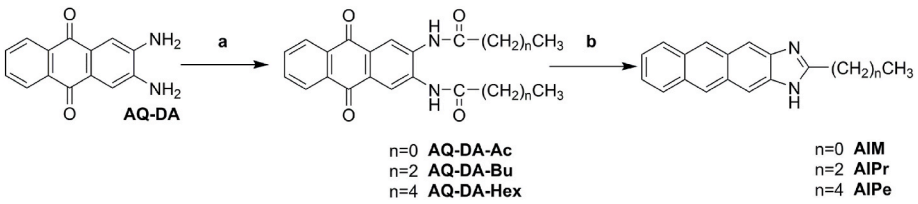

Scheme 2. Synthetic procedure for the preparation of the new anthraimidazole derivatives: a) the compound was reacted with the acetic, butyric or hexanoic anhydride in dry toluene at reflux overnight; b) the diamido compounds were refluxed in isopropanol for 16 h, in a basic environment and using $NaBH_4$ (in large excess) as reducing agent.

22.4, 25.0, 31.4, 36.7, 122.4, 127.2, 129.7, 133.7, 134.9, 135.5, 172.7, 182.1. FTIR (KBr, cm^{-1}): ν = 3425 (br, N–H), 3254, (C–H arom.), 2950 (C–H aliph.) 1673 (s, C═O), 1573 (m), 1335 (m), 1242 (m), 711 (m, C–H bending). Elemental analysis calcd for $C_{26}H_{32}N_2O_2$: C 77.19, H 7.97, N 6.92, found: C 77.31, H 7.93, N 6.88.

2.2.4. Synthesis of 2-methyl-1H-anthra [2,3-d]imidazole (AIM)

AQ-DA-Ac (0.820 g, 2.5 mmol) and sodium borohydride (5.7 g, 152 mmol) were mixed in a solution of isopropanol (10 mL) and sodium hydroxide (1.6 mL, 2 M). The reaction mixture was refluxed 16 h under nitrogen flux. Then, the green suspension was left cooled and poured in water (100 mL). The solid was recovered and poured in a solution diethyl ether (80 mL) and ethanol (40 mL). A greenish solid was filtered off and the filtrated solution was taken at reduced pressure (in a roto-evaporator) to remove all the solvent. The obtained solid was recovered by diethyl ether and filtered under vacuum. 483 mg of a yellow solid (**AIM**) was obtained. Yield 60 %.

M. p. 288 °C. **^{1}H-NMR** (500 MHz, DMSO-d_6) δ 2.58 (s, 3H); 7.37 (m, 2H); 7.97 (m, 2H); 8.11 (s, 2H); 8.61 (s, 2H); **^{13}C-NMR** (125 MHz, DMSO-d_6) δ 15.6, 109.2, 124.6, 125.6, 128.1, 130.0, 158.8. FTIR (KBr, cm^{-1}): ν = 3390 (br, N–H), 1646 (s, C═N), 1537 (m), 1414 (m), 889 (m), 736 (m, C–H bending). Elemental analysis calcd for $C_{16}H_{12}N_2$: C 82.73, H 5.21, N 12.06, found: C 82.87, H 5.25, N 11.99. HR-MS (ESI-IT-TOF]: calcd for $[C_{16}H_{12}N_2+H]^+$: 233.108; found $[M + H^+]^+$ = 233.107.

2.2.5. Synthesis of 2-propyl-1H-anthra [2,3-d]imidazole (AIPr)

The same procedure used for the synthesis of **AIM** was employed with the difference that **AQ-DA-Bu** was the starting compound. In the workup of the reaction, a further recrystallization step from ethanol/water was needed to obtain the pure compound. The yield was 30 %. M. p. 262 °C. **^{1}H-NMR** (500 MHz, DMSO-d_6) δ 0.94 (t, 3H, J = 7.5 Hz), 1.83 (m, 2H), 2.83 (t, 2H, J = 7.5 Hz); 7.33 (m, 2H); 7.95 (m, 2H); 8.09 (s, 2H); 8.59 (s, 2H); **^{13}C-NMR** (125 MHz, DMSO-d_6) δ 14.2, 21.0, 31.4105.0, 124.6, 125.6, 128.1, 129.4, 130.0, 162.3. FTIR (KBr, cm^{-1}): ν = 3433 (br, N–H), 2963 (C–H, aliph.), 1645 (s, C═N), 1533, 1419, 881, 737 (C–H bending). Elemental analysis calcd for $C_{18}H_{16}N_2$: C 83.04, H 6.19, N 10.76, found: C 83.15, H 6.25, N 10.56. HR-MS (ESI-IT-TOF]: calcd for $[C_{18}H_{16}N_2+H]^+$: 261.139; found $[M + H^+]^+$ = 261.137.

2.2.6. Synthesis of 2-pentyl-1H-anthra [2,3-d]imidazole (AIPe)

The same procedure used for the synthesis of **AIM** was employed with the difference that **AQ-DA-Hex** was the starting compound. In the workup of the reaction, a further recrystallization step from ethanol/water was needed to obtain the pure compound. The yield was 29 %. M. p. 242 °C. **^{1}H-NMR** (400 MHz, DMSO-d_6) δ 0.89 (t, 3H, J = 7.5 Hz), 1.36 (m, 4H), 1.87 (m, 2H), 2.91 (t, 2H, J = 7.5 Hz); 7.38 (m, 2H); 7.99 (m, 2H); 8.10 (s, 2H); 8.64 (s, 2H); **^{13}C-NMR** (100 MHz, DMSO-d_6) δ 14.3, 22.3, 27.3, 29.5, 31.4105.0, 124.6, 125.6, 128.1, 129.4, 130.0, 162.6. FTIR (KBr, cm^{-1}): ν = 3381 (br, N–H), 2919 (C–H, aliph.), 1646 (s, C═N), 1533 (m), 1416 (m), 890 (m), 736 (m, C–H) bending). Elemental analysis calcd for $C_{20}H_{20}N_2$: C 83.30, H 6.99, N 9.71, found: C 83.53, H 6.91, N 9.59 HR-MS (ESI-IT-TOF]: calcd for $C_{20}H_{20}N_2+H^+$: 289.170; found $[M + H^+]^+$ = 289.170.

2.3. DFT studies

All electronic computations have been carried out at the density functional level of theory (DFT) by using the B3LYP functional, together with the polarized 6–31 + G (d,p) basis set. That level of computations should provide reliable results, according to previous works [39,40]. Geometry optimizations and computations of normal coordinates and harmonic vibrational frequencies were carried out by using the Gaussian package (G16) [41]. To verify that the stationary points found were real minima on the potential energy surface, the calculation of the vibrational frequencies was carried out, and no imaginary values were found in any case. Time-dependent DFT (TDDFT) was employed for treating all excited states and to obtain the UV–Vis absorption spectra. Solvent (ethanol) effect has been included in the computation through the Polarizable Continuum Model (PCM), as implemented in the code Gaussian 16 [42]. The long alkyl chains were replaced by methyl groups in all the electronic computations, as routinely done in DFT studies [43].

2.4. X-Ray single crystal analysis

All data for crystal structure determinations were measured on a Bruker-Nonius KappaCCD diffractometer equipped with Oxford Cryostream 700 apparatus, using graphite mono-chromated MoKa radiation (0.71073 Å). Data were collected at −100 °C. Reduction of data and semiempirical absorption correction were performed using SADABS program [44]. The structures were solved by direct methods (SIR97 program) [45] and refined by the full-matrix least-squares method on F2 using SHELXL-2016 program [46] with the aid of the program WinGX [47]. H atoms bonded to C were generated stereochemically and refined by the riding model; those bonded to N were found in difference Fourier maps and their coordinates were refined. To all H atoms, U_{iso} equal to 1.2 times U_{eq} of the carrier atom was given. The analysis of the crystal packing was performed using the program Mercury [48].

3. Results and discussion

3.1. Synthesis

The starting compound for the synthesis of the new molecules was a commercial 2-aminoanthraquinone that, following a reported procedure, was transformed in three reaction steps to 2,3-diaminoanthraquinone **AQ-DA** [38]. We aimed to use **AQ-DA** as a precursor to prepare 2,3-diaminoanthracene, following a procedure described in a previous paper: this procedure consisted of the acylation of **AQ-DA** to obtain the diamido derivative, a reduction of anthraquinone to anthracene by using $NaBH_4$ and a final hydrolysis of the amido groups in basic conditions [37]. We therefore prepared **AQ-DA-Ac** (see Scheme 2) by treating **AQ-DA** with acetic anhydride in dry toluene. The diacetamido derivative was then reacted in isopropanol in a reducing environment, because of the presence of a large excess of $NaBH_4$, to obtain the corresponding 2,3-diacetamido anthracene compound. Surprisingly, the major product of the reaction was not the one expected but, as determined by a combined ^{1}H-NMR-Mass spectroscopy analysis, a new anthra [2,3-*d*]imidazole derivative: to our knowledge, this heterocycle has never been reported

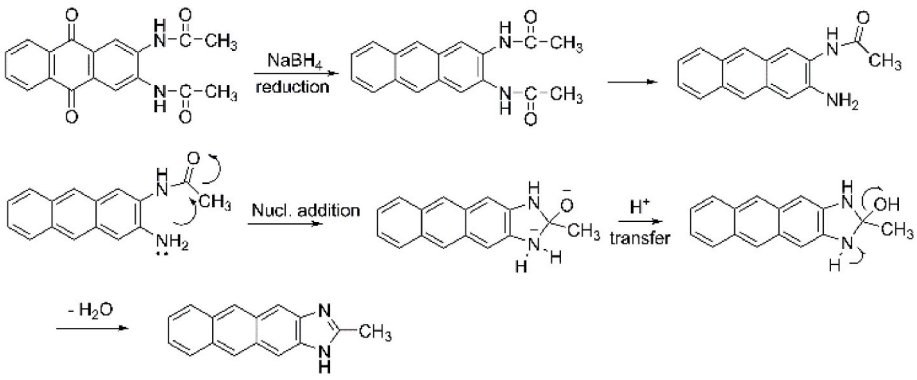

Scheme 3. Proposed mechanism for the formation of anthra [2,3-*d*]imidazole cycle.

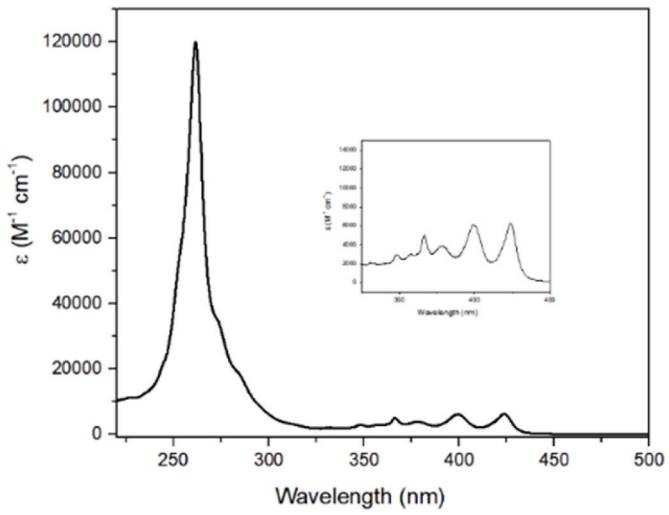

Fig. 1. Absorption spectrum of AIM in ethanol; in the inset, the vibronic structure of the peak at higher wavelength is shown.

in the literature. In Fig. S9 **^{1}H-NMR** spectrum of **AIM** (in DMSO-d_6) is shown: the aromatic zone of the spectrum is composed of four signals and a further singlet at 2.6 ppm: the latter integrates 1.5 five times each of the aromatic signals, so that the NMR spectrum cannot be assigned to the expected diacetamido compound (in that case, a 3/1 ratio should be observed). The spectrum is instead consistent with the structure proposed for **AIM** and the symmetric pattern obtained suggest that, in DMSO solution, the acidic proton of imidazole cycle is rapidly exchanged between the two nitrogens.

Mass spectrometry further confirms the chemical structure of **AIM** (see Fig. S11 in supporting information). The mechanistic hypothesis is shown in Scheme 3: we propose that diacetamido anthracene compound is initially formed (we manage to isolate it during the workout of the reaction, see Fig. S25); this derivative is then mono-hydrolysed in the strongly basic environment where the reaction takes place. Then a nucleophilic addition of the free amino group to the carbonyl group of the second acetamido group takes place, determining ring closure; loss of a water molecule finally afforded the anthraimidazole unit,

Table 2
Optical properties of AIM under different pH conditions.

Solution[a]	λ_{MAX} ^{abs} (nm)	λ_{MAX} ^{em} (nm)	Peak area[e]
pH 2	261/364/377/398/422	437/461[b]	2576
pH 3	261/364/377/398/422	437/461[b]	2506
pH 4	261/366/378/400/424	430/457/486[c]	2617
pH 7	261/366/378/400/424	430/457/486[c]	3043
pH 11	261/366/378/400/424	430/457/486[c]	3324
pH 12	262/366/373/400/424/451	430/457/489[d]	2542
pH 13	271/373/400/425/451	516[d]	2887

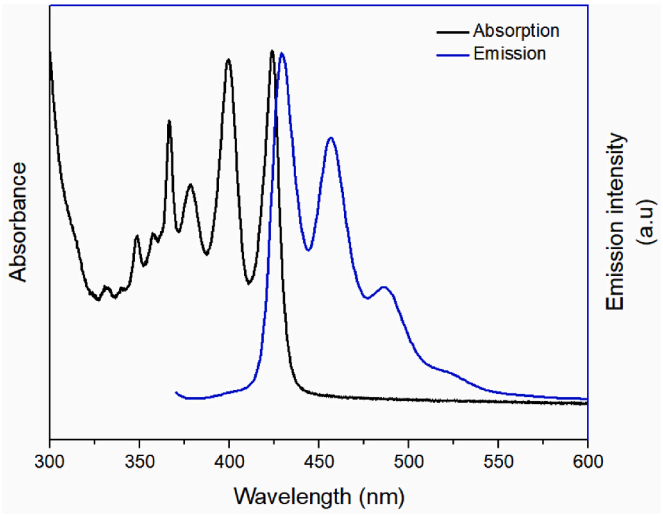

Fig. 2. Absorption (black line) and emission spectra (blue line) for AIM in ethanol solution.

substituted in position 1 with a methyl group. Indeed, in a recent work regarding the synthesis of 1-alkyl naphto [2–3,*d*]imidazole, a similar mechanism was hypothesized to explain the formation of the heterocycle and could validate the one here proposed [25]. The reaction proceeded with a satisfactorily yield of 60 %. To assess the generality of the reaction, we reacted **DA-AQ** with two further acid anhydrides,

Table 1
Optical properties of the synthesized molecules in ethanol solution.

	λ_1 (nm)/ε_1 ($M^{-1}cm^{-1}$)[a]	λ_2 (nm)/ε_2 ($M^{-1}cm^{-1}$)[a]	λ_3 (nm)/ε_3 ($M^{-1}cm^{-1}$)[a]	λ_4 (nm)/ε_4 ($M^{-1}cm^{-1}$)[a]	λ_5 (nm)/ε_5 ($M^{-1}cm^{-1}$)[a]	λ_{EM}(nm)[b]	Φ^c_{PL}
AIM	261/1.2•10^5	366/5.0•10^3	377/3.9•10^3	399/6.1•10^3	424/6.3•10^3	429/457/486	0.41
AIPr	262/1.2•10^5	367/5.5•10^3	378/4.0•10^3	400/6.0•10^3	425/6.1•10^3	430/458/487	0.40
AIPe	262/1.1•10^5	367/5.2•10^3	378/3.9•10^3	400/5.8•10^3	425/5.7•10^3	430/458/487	0.40

a) Measured in ethanol solution; b) excitation wavelength: 367 nm; c) Fluorescence quantum yield, measured using quinine sulphate as standard [49].

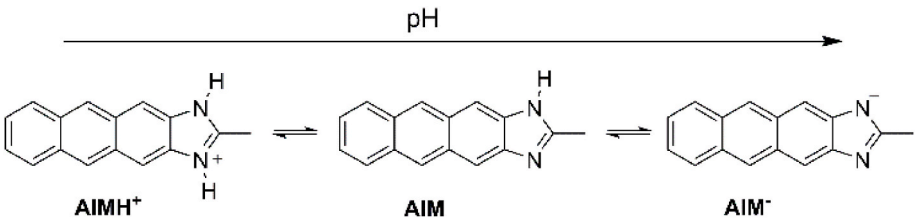

Fig. 3. Acid base equilibria involving **AIM**.

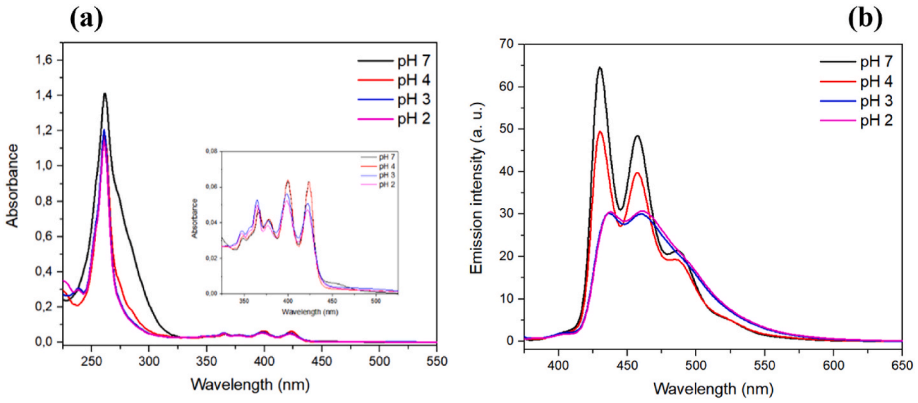

Fig. 4. (a) Absorption spectra of AIM in ethanol/water solutions (9/1 v/v) at different acid pH values. (b) Emission spectra of **AIM** in ethanol/water solutions (9/1 v/v) at different acid pH values.

bearing longer organic residues, obtaining **AQ-DA-Bu** and **AQ-DA-Hex** compounds. Also in these cases, the reaction with sodium borohydride afforded the anthrimidazole molecules (**AIPr** and **AIPe**), as determined by NMR (see Figs. S12–S13-S15-S16) and HR-MS analysis (see Figs. S14–S17), even though the higher solubility made necessary a further step of purification (by crystallization in ethanol/water) that reduced the yield to about 30 %.

3.2. Optical properties

The synthesized molecules were characterized regarding their optical absorption and fluorescence in ethanol solution. As expected, the three molecules show very similar optical behaviour; hence, we decided to focus the discussion on **AIM** molecule. Optical absorption spectrum for **AIM** is shown in Fig. 1 (optical absorption spectra of **AIPr** and **AIPe** are instead reported in Fig. S18): it is characterized by two main optical features, one more intense at 263 nm (ε higher than $1.1 \bullet 10^5$ $M^{-1}cm^{-1}$) and the second, at around 400 nm, featuring the typical vibronic structure of anthracene unit. Optical absorption properties are summarized in Table 1.

The same molecules were then characterized for what concerns their fluorescence properties as shown in Fig. 2 for **AIM** (and in Fig. S19 for **AIPr** and **AIPe**): upon excitation at 367 nm, the three molecules display a blue-colored emission, presenting a well-structured emission peak centered at around 460 nm. An interesting fluorescent quantum yield around 0.4 was measured by relative method, using quinine sulphate as standard Table 2.

The imidazole ring endowed the new anthraimidazole molecule with basic and acid functionalities as shown in Fig. 3, in fact, the pyridine-like basic nitrogen and a pyrrole-like acid N–H of **AIM** are involved in acid-base equilibria (see Fig. 3). To explore the possible use of the new derivatives as pH sensors, we thus investigated the optical behaviour of **AIM** under different pH conditions.

To investigate the optical behaviour in acid environment, **AIM** was solved in a mixture of ethyl alcohol and water (9/1 v/v ratio) containing HCl at three different concentrations, to achieve, respectively pH values

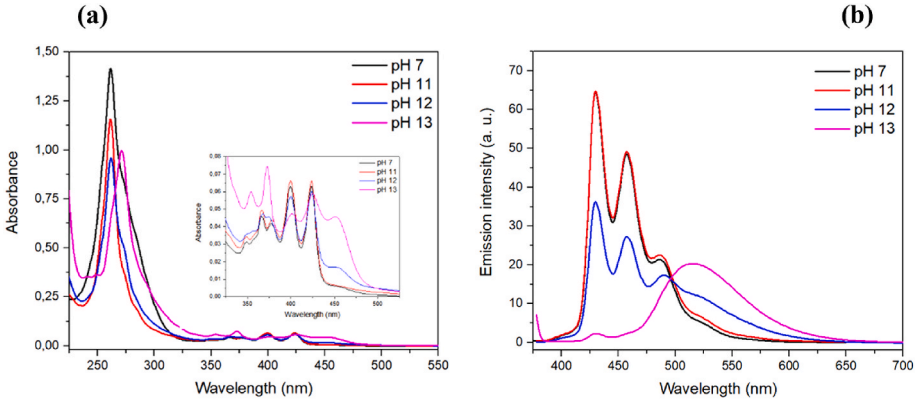

Fig. 5. (a) Absorption spectra of **AIM** in ethanol/water solutions (9/1 v/v) at different basic pH values. (b) Emission spectra of **AIM** in ethanol/water solutions (9/1 v/v) at different basic pH values.

of 2, 3 and 4. Optical absorption spectra of these three solutions are shown in Fig. 4a and compared with the spectrum of **AIM** dissolved in an aqueous ethanol solution of the same composition (9/1) but without any HCl (pH 7). In all the solution, **AIM** concentration was the same ($1\bullet10^{-5}$ M). As highlighted in the inset of Fig. 4a, optical absorption at pH 4 is virtually identical to that at pH 7, while at lower pH (3 and 2) a slight blue shift of the peaks at lower energy is observed. We deduced that below pH 4 the imidazolium form (**AIMH**$^+$, see Fig. 3) is prevalently present in the solution. Some differences can be observed in the emission spectra as well, as shown in Fig. 4b: below pH 4, emission becomes less structured and broader, and the emission wavelengths are slightly red shifted. By comparing the integrated area of the emission peaks, the fluorescence quantum yield in passing from the neutral to protonated form displays a 20 % decrease.

For what concerns the study of the optical behaviour in basic conditions, **AIM** was dissolved in an ethanol/water solution containing KOH at three different concentrations, so that the pH values were, respectively, 11, 12 and 13. Optical absorption spectra of these three solutions are shown in Fig. 5a and compared with the spectrum of **AIM** dissolved in an aqueous ethanol solution of the same composition (9/1) but without any KOH (pH 7). Once again, **AIM** concentrations were kept, in the different solutions, to the same value of $1\bullet10^{-5}$ M. In basic environment, more significant differences emerge. As highlighted in the insert of Fig. 5a, while at pH 11 the optical spectrum does not differ from that at pH 7, at higher pH values a new band at 450 nm appears and becomes more significant as the pH increases. The new band can be associated to the formation of the deprotonated form of **AIM** (**AIM**$^-$, imidazolate derivative) that, at pH 13, can be considered the prevalent species in solution. This behaviour seems to be consistent with the pK_a value reported for benzimidazole (pK_a for the neutral form of benzimidazole is reported to be 12.8) [50]. Because of the new band in the visible region, the color of the solutions at pH 13 becomes more neatly yellow. The same solutions were then studied regarding their fluorescence response, as shown in Fig. 5b. We can observe a dramatic change of the emission spectrum when the imidazolate form becomes prevalent, at pH 13: The addition of the base clearly modifies the emission spectrum: the spectrum becomes in fact featureless, with a unique broad peak centered at 516 nm. At pH 11 instead, the emission spectrum looks similar to that at pH 7, while at pH 12 an intermediate situation occurs, with a shoulder appearing at about 510 nm. Hence, the color emission sharply turns from blue to green in passing from pH11 to pH13: in this pH range it is evident that the emission at around 430 nm turns off, while it turns on at 516 nm. Interestingly, photoluminescent quantum yield in the deprotonated form of **AIM** (pH 13) is still strong, reducing by only 20 % as compared to the neutral form, as can be deduced from integrating the emission peaks at the different pH values. **AIM** hence proves to be a very alkaline pH sensor, able to clearly highlight pH change in a very narrow range. This optical behaviour is undoubtedly interesting, because pH sensors working in strong alkaline environments have rarely been reported in the literature [26,51,52] while it is known that this ability is highly required in several fields such as leather processing, wastewater treatment, paper industry, and metal mining and finishing [26].

a) Ethanol/water 9/1 solution, containing HCl (acid pH) or KOH (basic pH); b) excitation wavelength: 364 nm; b) excitation wavelength: 366 nm; d) excitation wavelength: 373 nm; e) integrated area of the emission peak.

3.3. DFT study

To get more information about the electronic structure of the synthesized dye, we have performed a computational analysis at the B3LYP/6-31 + G (d,p) level, including solvent effects (ethanol) through the polarizable continuum model. As commonly done in this kind of studies, the side alkyl chains have been modelled as a methyl group [40], since side chains are expected not to impact electronic properties [43]; this means that we have focused on **AIM** derivative only, in its neutral, basic (**AIM**$^-$) and acidic (**AIMH**$^+$) forms. The molecules have been optimized in their minimal energy structure, where they show a planar conformation. The predicted absorption spectra are reported in Supporting Information (Figs. S26–28). Wavelengths, energy, and oscillator strengths between ground state orbitals to the excited state are reported in Table S1. The theoretical spectrum in the fifty-excitation range explored by TD-DFT is made up of three principal bands, the highest one basically corresponding to a combination of HOMO - > LUMO+1 and HOMO - > LUMO+2 transition (see Table S1). A good qualitative accord with experimental behaviour (Fig. 1) is observed: the most intense optical transition, as well as the optical transitions in the visible range (as shown in Table S1), are red shifted for **AIM**$^-$ as compared to neutral and acidic form of the molecule. In Table 3 we report information about the main transitions as well as dipole moments of the ground state and of the first excited state, HOMO and LUMO energies. The former are in good agreement with the experiment, thus validating the calculation and the choice of the density functional used.

AIM shows a negligible increase in the overall dipole moment value when passing from ground to excited state. The density distribution of the orbitals involved in the main transitions visible in the UV spectra, i.e. HOMO-2, HOMO-1, HOMO, LUMO, LUMO+1 and LUMO+2 for **AIM** is shown in Fig. S29.

Table 3
Computed electronic and optical properties of the synthesized dye.

Dye	$\lambda_{abs,max}$ (nm)	F	μ (GS) (Debye)	μ (ES) (Debye)	HOMO (eV)	LUMO (eV)
AIM	267	2.53	5.64	5.85	−5.26	−2.07
AIMH$^+$	267	2.24	46.2	46.5	−5.81	−2.70
AIM$^-$	287	2.23	39.2	39.2	−4.52	−1.58

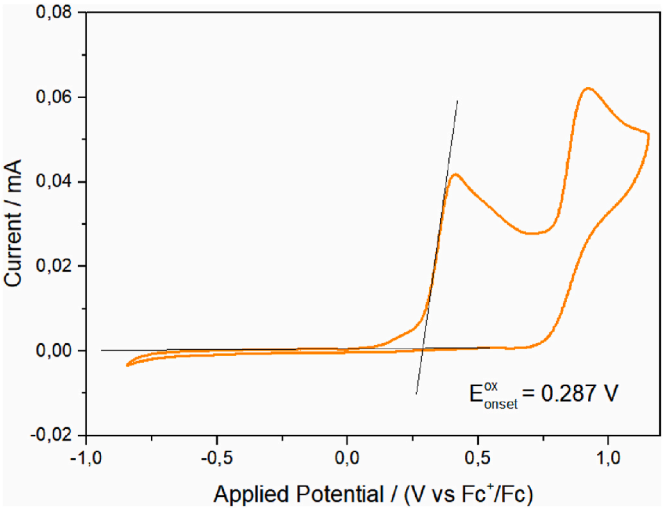

Fig. 6. Ciclovoltammetry plot of **AIM** in acetonitrile solution.

3.4. Electrochemical characterization

AIM molecule was electrochemically characterized by means of cyclic voltammetry (CV). The experiments were carried out in acetonitrile solution in inert environment. This kind of experiment provide useful information about the energies of frontier's molecular orbitals that can be related to oxidation (HOMO) and reduction (LUMO) potential of the investigated molecule, information that is of great importance in view of possible optoelectronic applications. CV graph is shown in Fig. 6.

The oxidation scan shows two peaks, the first irreversible and the

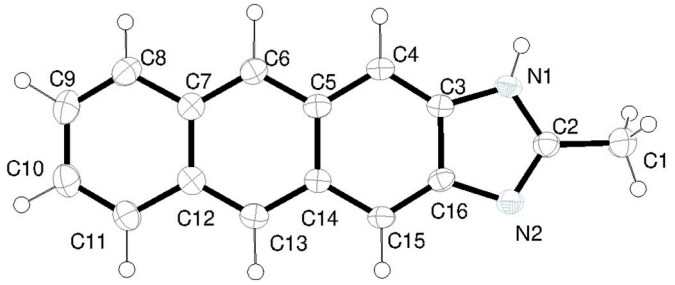

Fig. 7. **AIM** crystal structure. Ellipsoids are drawn at 50 % of probability level.

second quasi reversible. From the onset of the irreversible oxidation peak it is possible to determine HOMO energy of the molecule by applying the following equation [53].

$$E_{HOMO} = -\left(E^{ox}_{onset} + 5.1\right)(eV)$$

Where E^{ox}_{onset} represents the onset of oxidation potential (measured vs ferrocenium/ferrocenium oxidation potential). This equation is typically used when oxidation peak is irreversible as in the present case. HOMO energy of – 5.39 eV is obtained that is consistent with the calculated value of −5.26 eV. It was not possible to measure LUMO electrochemically because the reduction potential of **AIM** lies (as also the DFT computation suggest) outside the accessible potential window of the solvent.

3.5. Crystal structure

Dark green lozenge crystals of **AIM** were grown from slow evaporation of 1 mL of ethanol solution at room temperature in 2 days. **AIM** crystallizes in the orthorhombic space group *P*bca with Z = 8 (Fig. 7). The molecular backbone of the molecule is planar as it is typical for aromatic fused ring molecules.

Infinite ribbons of **AIM** molecules, almost perpendicular (72.04°) to each other, are held together by strong hydrogen bonding interactions between N1–H1···N2 (1.986 (2) Å) along the *a* axis (Fig. 8A). In this way, molecules are arranged in the crystal in a zig-zag fashioned motif with a stacking distance of two consecutive layers of 3.513 (2) Å (Fig. 8B). The angles and bond distances are in good agreement with the isostructural 2-methyl-1*H*-naphtoimidazole [25].

We also successfully solved the crystal structure of the protonated **AIM** with Bromide counterion (Fig. 9). Red needle-shaped crystals of **AIM-HBr** were grown by slow evaporation of 1 mL of ethanolic solution of **AIM** and 5 drops of 48 % hydrobromic acid solution at room temperature in five days. **AIM-HBr** crystallizes in the monoclinic space group with Z = 1.

The protonation of the molecular backbone occurs on the N2 atom of the imidazole ring. In this way infinite ribbons of AIM^{+} molecules oriented in head-tail motif along the *b* axis are held together by strong hydrogen bonds between the bromide counterions that act as bifurcated acceptor, as depicted in Fig. 10a (N1–H1···Br1 2.357 (3) Å N1–H2A … Br1 2.411 (4) Å). Along the *a* axis the molecules are arranged in an offset stacking (Fig. 10b) with shorter distance of the two layers than **AIM** crystal structure (3.387 (4) Å). The crystallographic data of both the crystal structures are reported in Tables S1–S2.

AIM and **AIM-HBr** crystal structure were deposited with the follow CCDC numbers 2339947, 2,339,953.

4. Conclusions

We reported in this paper the synthesis of three new molecules based on an unprecedented anthra [2,3-*d*]imidazole heterocycle. The new heterocycle unit has been serendipitously obtained while trying to reduce a 2,3-diamidoanthraquinone derivative to its anthracene analogue: we observed that, after the reduction, hydrolysis and cyclization occurred, affording the unexpected heterocycle. The chemical identity of the new molecules has been confirmed by a combined NMR and MS analysis. For one of the molecules, **AIM**, a DFT study has been

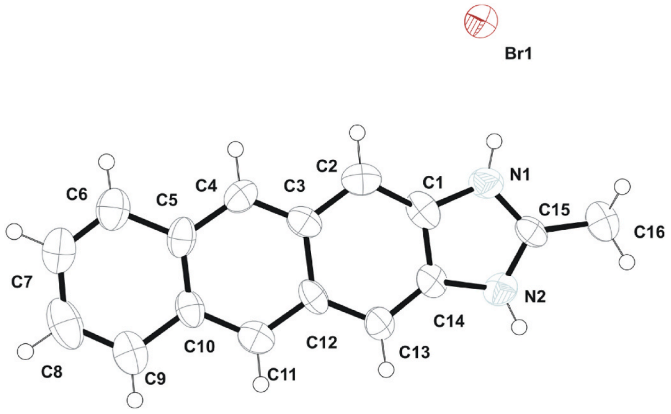

Fig. 9. AIM-HBr crystal structure. Ellipsoids are drawn at 50 % of probability level.

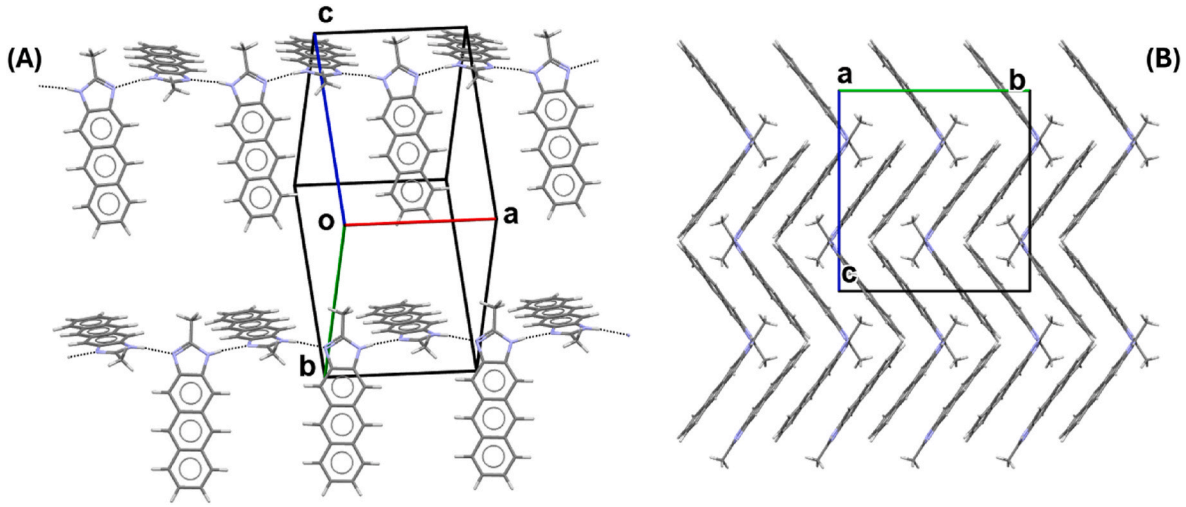

Fig. 8. Crystal packing of AIM crystal structure. A) Hydrogen bonding pattern in dashed black lines. B) View along *an* axis.

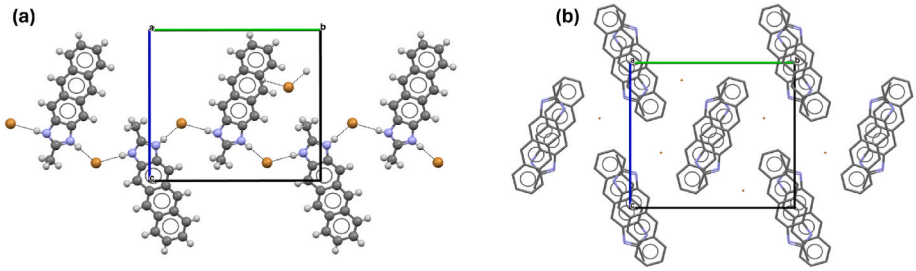

Fig. 10. Crystal packing of AIM-HBr. View along an axis: a) Hydrogen bonding pattern in dashed black lines. b) Off-set stacking visualization, H atoms are omitted for clarity.

performed, and single crystals suitable for XRD analysis were obtained and the structure solved, definitively proving the formation of the new unit. The fused heterocycle is, as expected, planar and crystal packing is characterized by infinite ribbons of **AIM** molecules held together by strong hydrogen bonding interactions involving the two different types of nitrogen on imidazole ring and arranged to form a zig-zag motif. The anthraimidazole cycle is characterized, on the imidazole ring, by acid (pyrrole-like NH) and basic (pyridine-like N) functionalities. We manage to obtain single crystals of a hydrobromide derivative of **AIM**, and its crystal structure as well was solved by means of XRD. All the new molecules were characterized regarding optical properties: all of them present a strong blue emission in ethanol solution, with a fluorescence quantum yield around 0.40. Moreover, the optical response of **AIM** molecule at different pH was investigated. A slight change in both optical absorption and emission spectra was observed at pH lower than 4, where the molecule is prevalently in its protonated form. More significant variations appear instead at basic pH: a new absorption band appears when pH 12 that became more intense at pH13, where **AIM** exists prevalently in its deprotonated form. The differences are even more significant for what concerns fluorescence properties: in passing from pH 11 (where the neutral form of **AIM** is still prevalent) to pH 13, the emission spectrum is significantly red-shifted and the color turns from blue to green. Moreover, fluorescence quantum yield diminishes only slightly in passing from the neutral to the deprotonated form. The peculiar optical properties at high pH values makes the new class of derivatives here reported very promising in the field of pH sensors working under very alkaline conditions.

Supporting information

^{1}H NMR, ^{13}C NMR, FTIR, ESI-IT-TOF Mass spectra, and DSC thermograms as well as crystallographic data of **AIM** and **AIM-HBr** can be found in Supporting Information. Predicted absorption spectra of AIM in its neutral, basic and protonated forms and the electron density distribution of the orbitals involved in the main optical transistion are also reported in the Supporting Information.

Funding

We acknowledge for financial support PRIN 2022 Grant 2022XSC9P5 (INTESA-SOLE) awarded by Italian Ministry of University and Research (MUR) in the framework of the National Recovery and Resilience Plan (NRRP), Mission 4, Component 2, Investment 1.1, Call for tender No. 104 published on February 2, 2022, funded by the European Union – NextGenerationEU.

CRediT authorship contribution statement

Emmanuele Parisi: Writing – review & editing, Writing – original draft, Investigation, Data curation, Conceptualization. **Emanuela Santagata:** Writing – original draft, Investigation. **Alessandro Landi:** Data curation, Investigation, Writing – review & editing. **Roberto Centore:** Writing – review & editing, Supervision, Data curation. **Marco Chino:** Writing – review & editing, Investigation, Data curation. **Antonio Carella:** Writing – review & editing, Writing – original draft, Supervision, Investigation, Funding acquisition, Data curation, Conceptualization.

Declaration of competing interest

The authors declare that they have no known competing financial interests or personal relationships that could have appeared to influence the work reported in this paper.

Data availability

Data will be made available on request.

Appendix A. Supplementary data

Supplementary data to this article can be found online at https://doi.org/10.1016/j.dyepig.2024.112440.

References

[1] Becker HD. Unimolecular photochemistry of anthracenes. Chem Rev. 1993;93:145–72. https://doi.org/10.1021/CR00017A008/ASSET/CR00017A008.FP.PNG_V03.
[2] Lim H, Woo S-J, Ha H, Kim Y-H, Kim J-J, Lim H, et al. Breaking the efficiency limit of deep-blue fluorescent OLEDs based on anthracene derivatives. Adv Mater 2022;34:2100161. https://doi.org/10.1002/ADMA.202100161.
[3] Aydemir M, Haykir G, Battal A, Jankus V, Sugunan SK, Dias FB, et al. High efficiency OLEDs based on anthracene derivatives: the impact of electron donating and withdrawing group on the performance of OLED. Org Electron 2016;30:149–57. https://doi.org/10.1016/J.ORGEL.2015.11.026.
[4] Ha JM, Hur SH, Pathak A, Jeong JE, Woo HY. Recent advances in organic luminescent materials with narrowband emission. NPG Asia Mater 2021;13(1):1–36. https://doi.org/10.1038/s41427-021-00318-8. 2021;13.
[5] Park H, Lee J, Kang I, Chu HY, Lee JI, Kwon SK, et al. Highly rigid and twisted anthracene derivatives: a strategy for deep blue OLED materials with theoretical limit efficiency. J Mater Chem 2012;22:2695–700. https://doi.org/10.1039/C2JM16056K.
[6] Banthia S, Samanta A. A new strategy for ratiometric fluorescence detection of transition metal ions. J Phys Chem B 2006;110:6437–40. https://doi.org/10.1021/JP060767Z/SUPPL_FILE/JP060767ZSI20060206_075713.PDF.
[7] Razavi B, Roghani-Mamaqani H, Salami-Kalajahi M. Development of highly sensitive metal-ion chemosensor and key-lock anticounterfeiting technology based on oxazolidine. Sci Rep 2022;12(12):1–10. https://doi.org/10.1038/s41598-022-05098-x. 1 2022.
[8] Kumar G, Srivastava A, Kumar P, Srikrishna S, Singh VP. Fluorescent turn-on anthracene-based aluminum(III) sensor for a therapeutic study in alzheimer's disease model of Drosophila. ACS Chem Neurosci 2023;14:2792–801. https://doi.org/10.1021/ACSCHEMNEURO.3C00340/ASSET/IMAGES/LARGE/CN3C00340_0008.JPEG.
[9] Chi KM, Frerichs SB, Philson SR, Ellis JE, Jonas C-C, Hiselhoff K, Goddard Kruger Inorg Chini Actu RC, I YX, et al. An anthracene-based fluorescent sensor for transition metal ions. Angew Chem Int Ed Engl 1994;33:1975–7. https://doi.org/10.1002/ANIE.199419751.
[10] Tümay SO, Irani-nezhad MH, Khataee A. Design of novel anthracene-based fluorescence sensor for sensitive and selective determination of iron in real samples. J Photochem Photobiol Chem 2020;402:112819. https://doi.org/10.1016/J.JPHOTOCHEM.2020.112819.

[11] Ghosh K, Masanta G. Anthracene-based open and macrocyclic receptors in the flurometric detection of urea. New J Chem 2009;33:1965–72. https://doi.org/10.1039/B909536E.

[12] Fabbrizzi L, Licchelli M, Perotti A, Poggi A, Rabaioli G, Sacchi D, et al. Fluorescent molecular sensing of amino acids bearing an aromatic residue. Journal of the Chemical Society, Perkin Transactions 2001;1:2108–13. https://doi.org/10.1039/B105480P. 2.

[13] Chen M, Yan L, Zhao Y, Murtaza I, Meng H, Huang W. Anthracene-based semiconductors for organic field-effect transistors. J Mater Chem C Mater 2018;6:7416–44. https://doi.org/10.1039/C8TC01865K.

[14] Liu J, Zhang H, Dong H, Meng L, Jiang L, Jiang L, et al. High mobility emissive organic semiconductor. Nat Commun 2015;6(6):1–8. https://doi.org/10.1038/ncomms10032. 1 2015.

[15] Chung DS, An TK, Park CE, Yun HJ, Kwon SK, Kim YH. High-speed solution-processed organic single crystal transistors using a novel triisopropylsilylethynyl anthracene derivative. Appl Phys Lett 2012;101:193304. https://doi.org/10.1063/1.4764062/127689.

[16] Liu J, Dong H, Wang Z, Ji D, Cheng C, Geng H, et al. Thin film field-effect transistors of 2,6-diphenyl anthracene (DPA). Chem Commun 2015;51:11777–9. https://doi.org/10.1039/C4CC10348C.

[17] Li J, Zhou K, Liu J, Zhen Y, Liu L, Zhang J, et al. Aromatic extension at 2,6-positions of anthracene toward an elegant strategy for organic semiconductors with efficient charge transport and strong solid state emission. J Am Chem Soc 2017;139:17261–4. https://doi.org/10.1021/JACS.7B09381/ASSET/IMAGES/LARGE/JA-2017-093819_0004.JPEG.

[18] Dadvand A, Moiseev AG, Sawabe K, Sun W-H, Djukic B, Chung I, et al. Maximizing field-effect mobility and solid-state luminescence in organic semiconductors. Angew Chem Int Ed 2012;51:3837–41. https://doi.org/10.1002/ANIE.201108184.

[19] Niimi K, Miyazaki E, Osaka I, Takimiya K. Facile syntheses of anthra[2,3-b] chalcogenophenes. Synthesis 2012;44:2102–6. https://doi.org/10.1055/S-0031-1291141.

[20] Nakano M, Niimi K, Miyazaki E, Osaka I, Takimiya K. Isomerically pure anthra[2,3-b:6,7-b']-difuran (anti-ADF), -dithiophene (anti-ADT), and -diselenophene (anti-ADS): selective synthesis, electronic structures, and application to organic field-effect transistors. J Org Chem 2012;77:8099–111. https://doi.org/10.1021/JO301438T/SUPPL_FILE/JO301438T_SI_002.CIF.

[21] Tang ML, Okamoto T, Bao Z. High-performance organic semiconductors: asymmetric linear acenes containing sulphur. J Am Chem Soc 2006;128:16002–3. https://doi.org/10.1021/JA066824J/SUPPL_FILE/JA066824JSI20060921_121821.PDF.

[22] Parisi E, Carella A, Borbone F, Chiarella F, Gentile FS, Centore R. Effect of chalcogen bonding on the packing and coordination geometry in hybrid organic–inorganic Cu(II) networks. CrystEngComm 2022;24:2884–90. https://doi.org/10.1039/D2CE00069E.

[23] Centore R, Borbone F, Carella A, Causà M, Fusco S, Gentile FS, et al. Hierarchy of intermolecular interactions and selective topochemical reactivity in different polymorphs of fused-ring heteroaromatics. Cryst Growth Des 2020;20:1229–36. https://doi.org/10.1021/ACS.CGD.9B01491/ASSET/IMAGES/LARGE/CG9B01491_0008.JPEG.

[24] Gentile FS, Parisi E, Centore R. Journeys in crystal energy landscapes: actual and virtual structures in polymorphic 5-nitrobenzo[c][1,2,5]thiadiazole. CrystEngComm 2023;25:859–65. https://doi.org/10.1039/D2CE01619B.

[25] Siddiqui ZA, Lambud S, Bhadke A, Kumar R, Prajesh N, Sekar N, et al. Unexpected formation of 2-methyl-1H-naphtho [2, 3-d] imidazole via decarboxylation governed mechanistic pathway. Chem Phys 2023;565:111735. https://doi.org/10.1016/j.chemphys.2022.111735.

[26] Zhu X, Lin Q, Zhang YM, Wei TB. Nitrophenylfuran-benzimidazole-based reversible alkaline fluorescence switch accurately controlled by pH. Sens Actuators B Chem. 2015;219:38–42. https://doi.org/10.1016/J.SNB.2015.05.004.

[27] Alghamdi SS, Suliman RS, Almutairi K, Kahtani K, Aljatli D. Imidazole as a promising medicinal scaffold: current status and future direction. Drug Des Dev Ther 2021;15:3289–312. https://doi.org/10.2147/DDDT.S307113.

[28] Teli P, Sahiba N, Sethiya A, Soni J, Agarwal S. Imidazole derivatives: impact and prospects in antiviral drug discovery. Elsevier; 2021. https://doi.org/10.1016/B978-0-323-85479-5.00001-0.

[29] Ye S, Zhuang S, Pan B, Guo R, Wang L. Imidazole derivatives for efficient organic light-emitting diodes. Journal of Information Display 2020;21:173–96. https://doi.org/10.1080/15980316.2020.1802357.

[30] Tagare J, Vaidyanathan S. Recent development of phenanthroimidazole-based fluorophores for blue organic light-emitting diodes (OLEDs): an overview. J Mater Chem C Mater 2018;6:10138–73. https://doi.org/10.1039/C8TC03689F.

[31] Subeesh MS, Shanmugasundaram K, Sunesh CD, Nguyen TP, Choe Y. Phenanthroimidazole derivative as an easily accessible emitter for non-doped light-emitting electrochemical cells. J Phys Chem C 2015;119:23676–84. https://doi.org/10.1021/ACS.JPCC.5B07871/ASSET/IMAGES/LARGE/JP-2015-07871S_0002. JPEG.

[32] Nemati Bideh B, Moghadam M, Sousaraei A, Shahpoori Arani B. Phenanthroimidazole as molecularly engineered switch for efficient and highly long-lived light-emitting electrochemical cell. Sci Rep 2023;13(1):1–11. https://doi.org/10.1038/s41598-023-29527-7. 2023;13.

[33] Szlapa-Kula A, Kula S. Progress on phenanthroimidazole derivatives for light-emitting electrochemical cells: an overview. Energies 2023;16:5194. https://doi.org/10.3390/EN16135194. 2023;16:5194.

[34] Beneto AJ, Thiagarajan V, Siva A. A tunable ratiometric pH sensor based on phenanthro[9,10- d]imidazole covalently linked with vinylpyridine. RSC Adv 2015;5:67849–52. https://doi.org/10.1039/C5RA09536K.

[35] Cheng F, Tang N, Chen J, Chen G. Luminescent pH sensor of a novel imidazole-containing hexanuclear Ru(II) polypyridyl complex. Spectrochim Acta Mol Biomol Spectrosc 2013;114:159–63. https://doi.org/10.1016/J.SAA.2013.05.059.

[36] Zhao B, Fang Y, Xu Y, Deng Q, Liu T, Kan W, et al. Dual-responsive pH sensor based on a phenanthro[9,10-d]imidazole fluorophore modified by amino diacetate. Tetrahedron Lett 2016;57:1825–30. https://doi.org/10.1016/J.TETLET.2016.03.046.

[37] Kantam R, Holland R, Khanna BP, Revell KD. An optimized method for the synthesis of 2,6-diaminoanthracene. Tetrahedron Lett 2011;52:5083–5. https://doi.org/10.1016/J.TETLET.2011.07.106.

[38] Kolmer-Anderl N, Kolmer A, Thiele CM, Rehahn M. Exploration of the photodegradation of naphtho[2,3-g] quinoxalines and pyrazino[2,3-b]phenazines. Chem Eur J 2016;22:5277–87. https://doi.org/10.1002/CHEM.201504453.

[39] Landi A, Landi A, Velardo A, Peluso A. Efficient charge dissociation of triplet excitons in bulk heterojunction solar cells. ACS Appl Energy Mater 2022;5:10815–24. https://doi.org/10.1021/ACSAEM.2C01495/ASSET/IMAGES/MEDIUM/AE2C01495_M021.GIF.

[40] Landi A, Padula D. Multiple charge separation pathways in new-generation non-fullerene acceptors: a computational study. J Mater Chem A Mater 2021;9:24849–56. https://doi.org/10.1039/D1TA05664F.

[41] Frisch MJ, et al. Gaussian 16, revision A.03. 2016.

[42] Miertuš S, Scrocco E, Tomasi J. Electrostatic interaction of a solute with a continuum. A direct utilizaion of AB initio molecular potentials for the prevision of solvent effects. Chem Phys 1981;55:117–29. https://doi.org/10.1016/0301-0104(81)85090-2.

[43] Paternò GM, Barbero N, Galliano S, Barolo C, Lanzani G, Scotognella F, et al. Excited state photophysics of squaraine dyes for photovoltaic applications: an alternative deactivation scenario. J Mater Chem C Mater 2018;6:2778–85. https://doi.org/10.1039/C7TC05078J.

[44] Bruker-Nonius. SADABS, bruker-nonius. 2002. Delft, The Netherlands.

[45] Altomare A, Burla MC, Camalli M, Cascarano GL, Giacovazzo C, Guagliardi A, et al. SIR97: a new tool for crystal structure determination and refinement. J Appl Crystallogr 1999;32:115–9. https://doi.org/10.1107/S0021889898007717.

[46] Sheldrick GM. Crystal structure refinement with SHELXL. Acta Crystallogr C Struct Chem 2015;71:3–8. https://doi.org/10.1107/S2053229614024218.

[47] Farrugia LJ. WinGX and ORTEP for windows: an update. J Appl Crystallogr 2012;45:849–54. https://doi.org/10.1107/S0021889812029111.

[48] Macrae CF, Bruno IJ, Chisholm JA, Edgington PR, McCabe P, Pidcock E, et al. Mercury CSD 2.0 - new features for the visualization and investigation of crystal structures. J Appl Crystallogr 2008;41:466–70. https://doi.org/10.1107/S0021889807067908.

[49] Melhuish WH. Quantum efficiencies of fluorescence of organic substan ces: effect of solvent and concentration of the fluorescent solute. J Phys Chem 1961;65:229–35. https://doi.org/10.1021/J100820A009/ASSET/J100820A009.FP.PNG_V03.

[50] Walba H, Isensee RW. Acidity constants of some arylimidazoles and their cations. J Org Chem 1961;26:2789–91. https://doi.org/10.1021/JO01066A039/ASSET/JO01066A039.FP.PNG_V03.

[51] Zhang F, Dong W, Ma Y, Jiang T, Liu B, Li X, et al. Fluorescent pH probes for alkaline pH range based on perylene tetra-(alkoxycarbonyl) derivatives. Arab J Chem 2020;13:5900–10. https://doi.org/10.1016/J.ARABJC.2020.04.033.

[52] Lee H, Lee S, Han MS. Turn-on fluorescent pH probes for monitoring alkaline pHs using bis[2-(2′-hydroxyphenyl)benzazole] derivatives. Sensors 2023;23:2044. https://doi.org/10.3390/S23042044/S1.

[53] Cardona CM, Li W, Kaifer AE, Stockdale D, Bazan GC. Electrochemical considerations for determining absolute frontier orbital energy levels of conjugated polymers for solar cell applications. Adv Mater 2011;23:2367–71. https://doi.org/10.1002/adma.201004554.